Nano Research

ISSN 1998-0124 CN 11-5974/O4
https://doi.org/10.1007/s12274-023-5420-1

Research Article

Miniaturized retractable thin-film sensor for wearable multifunctional respiratory monitoring

Chengyu Li[1,2,§], Zijie Xu[1,2,§], Shuxing Xu[1,3,§], Tingyu Wang[1,2], Siyu Zhou[4], Zhuoran Sun[4], Zhong Lin Wang[1,5] (✉), and Wei Tang[1,2,3] (✉)

[1] *Beijing Institute of Nanoenergy and Nanosystems, Chinese Academy of Sciences, Beijing 101400, China*
[2] *School of Nanoscience and Technology, University of Chinese Academy of Sciences, Beijing 100049, China*
[3] *Center on Nanoenergy Research, School of Physical Science and Technology, Guangxi University, Nanning 530004, China*
[4] *Peking University Third Hospital, Beijing 100191, China*
[5] *Georgia Institute of Technology, Atlanta, GA 30332, USA*
[§] *Chengyu Li, Zijie Xu, and Shuxing Xu contributed equally to this work.*

Received: 11 October 2022 / **Revised:** 18 November 2022 / **Accepted:** 18 December 2022

ABSTRACT

As extremely important physiological indicators, respiratory signals can often reflect or predict the depth and urgency of various diseases. However, designing a wearable respiratory monitoring system with convenience, excellent durability, and high precision is still an urgent challenge. Here, we designed an easy-fabricate, lightweight, and badge reel-like retractable self-powered sensor (RSPS) with high precision, sensitivity, and durability for continuous detection of important indicators such as respiratory rate, apnea, and respiratory ventilation. By using three groups of interdigital electrode structures with phase differences, combined with flexible printed circuit boards (FPCBs) processing technology, a miniature rotating thin-film triboelectric nanogenerator (RTF-TENG) was developed. Based on discrete sensing technology, the RSPS has a sensing resolution of 0.13 mm, sensitivity of 7 $P \cdot mm^{-1}$, and durability more than 1 million stretching cycles, with low hysteresis and excellent anti-environmental interference ability. Additionally, to demonstrate its wearability, real-time, and convenience of respiratory monitoring, a multifunctional wearable respiratory monitoring system (MWRMS) was designed. The MWRMS demonstrated in this study is expected to provide a new and practical strategy and technology for daily human respiratory monitoring and clinical diagnosis.

KEYWORDS

respiratory monitoring, thin-film sensors, discrete and vector, self-powered, triboelectric nanogenerator

1 Instruction

Respiratory diseases such as sleep apnea syndrome, asthma, and chronic obstructive pulmonary disease (COPD) are becoming a growing global and serious health problem. According to statistics, COPD and asthma, two major respiratory diseases, affect more than 435 million people worldwide, consuming medical costs of $50 billion per year [1–3]. It is worth noting that COVID-19 which outbroke in 2019, is also highly susceptible to respiratory damage [4, 5]. In this case, daily respiration monitoring becomes particularly urgent, and any changes in respiratory conditions should be treated promptly and effectively to prevent further deterioration [6–8].

Currently, the clinical approach to respiratory monitoring consists of two main methods: invasive and non-invasive. The former includes endotracheal intubation and tracheotomy, and the latter includes mask ventilation [9, 10]. Since the high cost, low comfort, limited site, and inflexibility of operation of the above two methods are difficult to effectively apply to daily life and portable medical monitoring. However, the rapid growth of electronic information, wireless communication, and human–computer interaction has effectively promoted the development of wearable electronics in the medical field [11, 12]. Recently, research on wearable respiratory monitoring devices has made great progress [13–15], which can be divided into direct and indirect monitoring. Direct respiratory monitoring is achieved mainly through detecting humidity, air pressure, and temperature of exhaled breath [16, 17], which is susceptible to environmental interference, resulting in lower accuracy and increased noise [14, 18]. As for indirect respiratory monitoring, strain or pressure sensors are mostly used, mainly utilizing stretchable electrodes or functional materials adhering to the skin surface of the chest and abdomen [8, 19, 20]. However, long-time attaching might lead to skin allergies, redness, and other inflammatory reactions, affecting the monitoring signal. Thus, it is desperately desirable to develop a wearable respiratory monitoring system with more practical.

As an emerging self-powered sensing method, wearable technology based on triboelectric nanogenerators (TENGs) has recently attracted widespread attention [21, 22]. Many researchers have shown that TENG-based wearable sensors are a promising solution for respiratory monitoring [23–25], e.g., Zhou et al. designed a composite structure of stretchable and multi-channel

Address correspondence to Zhong Lin Wang, zlwang@gatech.edu; Wei Tang, tangwei@binn.cas.cn

bionic respiratory monitoring sensor inspired by the shark gill cleft structure [11]. Peng et al. developed a polyamide 66/Au-based nanofiber electronic skin with excellent power density and pressure sensitivity for respiratory monitoring by contact-separation mode TENG [19]. Fang et al. proposed a textile-based TENG sensing network with high sensitivity and fast response time, which enables effective recognition of breathing patterns via machine learning [10]. These devices have greatly facilitated the development of wearable self-powered sensors for physiological signal monitoring, but there are also some challenges, including environmental temperature and humidity influence, as well as durability. Few TENG-based respiratory sensors reach 50,000 stretch cycles, while a healthy human breathes about 28,000 times per day [26–29]. Therefore, a respiratory monitoring sensor with interference resistance and ultrahigh durability is in demand.

In this work, we have reported a miniature rotating thin-film TENG (RTF-TENG) with a film thickness of 0.2 mm and an area of 1.2 cm^2 via flexible printed circuit board (FPCB) processing technology. The ingenious application of three sets of forked finger electrode structures with phase differences on the stator FPCB gives it high precision (0.13 mm) and vector sensing capability. Besides, inspired by the badge reel structure, via embedding a RTF-TENG into a three-dimensional (3D) printing structure, a badge reel-like retractable self-powered sensor (RSPS) has been developed (< 1.8 g). Since the fully encapsulated package and discrete measurement method, the sensor has excellent resistance to environmental temperature and humidity interference. The RSPS shows a sensitivity of 7 $P{\cdot}mm^{-1}$ (P represents peaks), temperature drift coefficient of 700 $ppm{\cdot}°C^{-1}$, and over 1 million stretching cycles. Furthermore, by designing a wireless acquisition circuit and interconnecting it with RSPS and an adjustable nylon strap, a wireless multifunctional wearable respiratory monitoring system (MWRMS) was developed to achieve daily respiratory monitoring. The MWSRS has been used continuously to measure respiratory rate (RF), one-second respiratory rate, apnea, and apnea count, validating its capabilities of daily portable monitoring.

2 Results and discussion

2.1 The concept, structure, and working principle of the sensing system

A wearable respiratory monitoring belt (chest strap) has been developed to make respiratory testing convenient and comfortable. Figure 1(a) depicts a chest strap diagram, with the upper inset's basic waveform output and the optical schematic of the respiratory monitoring belt in the lower inset. The exploded view is shown in Fig. 1(b), which represents the strap consisting of adjustable nylon straps, RSPSs, and multi-channel wireless acquisition circuits. Through a 3D printing shell, the RSPS and the acquisition circuit were assembled together. Specifically, the RSPS is similar to a badge reel and composed of a rotor, a stator, and a cover. The friction contact part of the rotor and the stator was attached with a RTF-TENG. The detailed production process of the respiratory monitoring belt is shown in Fig. S1 in the Electronic Supplementary Material (ESM). RTF-TENG consists of a rotor FPCB, a stator FPCB (both FPCB thicknesses: ~ 0.1 mm), and Kapton friction layer (thickness: ~ 25 μm), as shown in the inserted optical photograph. The stator FPCB is made up of three groups of interdigitated electrode structures with phase differences, and the number of electrodes of the rotor FPCB is one-third of that of the stator FPCB, and thus the output voltage of the designed device can generate three groups of independent and phase-differenced alternating current (AC) voltage signals.

Additionally, to realize the wireless communication of respiration signal, we designed a circuit containing the WiFi module controlled by STM32, analog-to-digital (AD) acquisition module, and charge amplifier, etc. (Fig. 1(c)). It is notable that the RTF-TENG, working in three-electrode (TE) mode, optimizes the entire sensor in terms of small size and weight, high precision, and vector sensing ability. As shown in Fig. 1(d), the diameter of the packaged sensor is about 20 mm, with a thickness of 5.9 mm and a mass of less than 1.8 g. Moreover, we have also compared and investigated the different working principles of retractable sensors. As shown in Fig. 1(e), the characteristics of the RSPS were compared with resistive, capacitive, triboelectricity, optical, and thermal effect-based stretchable (or strain) sensors in terms of tensile cycles and measured resolution [26, 27, 30–40]. The RSPS proposed in this research exhibits higher durability (1 million continuous stretching cycles) and resolution (arc length: ~ 0.13 mm), demonstrating the advantages of the device as a wearable sensor for sensing slight stretch such as breathing. Unlike conventional grating sensors that require power supply, are bulky, and have complex structures, our proposed self-powered RTF-TENG has easier processing and is lightweight (Fig. 1(f)(i)). Meanwhile, compared with the freestanding triboelectric-layer (FT) mode TENG sensors, which do not have vector sensing capability and have lower accuracy, and the current TENG-based vector sensors, RTF-TENG gives higher precision and smaller size due to the TE operating structure with a phase difference (Figs. 1(f)(ii)) and 1(f)(iii))) and more information shown in Fig. S2 in the ESM).

2.2 The working principle and output performance of RSPS

The RSPS is mainly composed of RTF-TENG. When the rope is stretched and contracted, the rotor rotates clockwise and counterclockwise relative to the stator. The rotor FPCB in the middle of the rotor and stator rubs against the Kapton film, which alternately induces a corresponding charge on the stator FPCB grating electrode and outputs an AC signal to the outside. The detailed mechanical working principle of the sensor is shown in Fig. S3 in the ESM. In particular, as shown in Fig. 2(a), the working principle of RTF-TENG during rotation differs from the FT mode of TENG. Owing to the coupling of triboelectric charging and electrostatic induction, when the rotor rotates on the Kapton film with contact friction, each group of stators grating electrodes at the bottom induces charges alternately, and three groups of independent AC voltage signals can be output when there is an external load.

To investigate the TE and FT modes of TENG, we designed two simplified models of the toroidal planar structure and simulated them separately via COMSOL software. The simulated structures and potential distributions of TENG's TE and FT modes are shown in Fig. 2(b), where their electrode widths and spacings are set to 10°. Furthermore, we also explored the simulation output of TENG in FT and TE modes controlling the same dimensions and the same rotation angles (from 90° to 360°), as shown in Fig. 2(c) and Fig. S4 in the ESM. The result indicates that TE mode TENG can obtain two times the number of peaks (NOPs) (including peaks and troughs) compared to the FT-TENG under the same rotation angle, endowing it with higher precision and sensitivity (Movie ESM1). In addition, we also simulated and analyzed the TE-based TENG output voltage with different electrode widths (more details are available in Fig. S5 in the ESM), demonstrating that the simulated output voltage increases with increasing electrode width.

Subsequently, we examined the characterization of RSPS

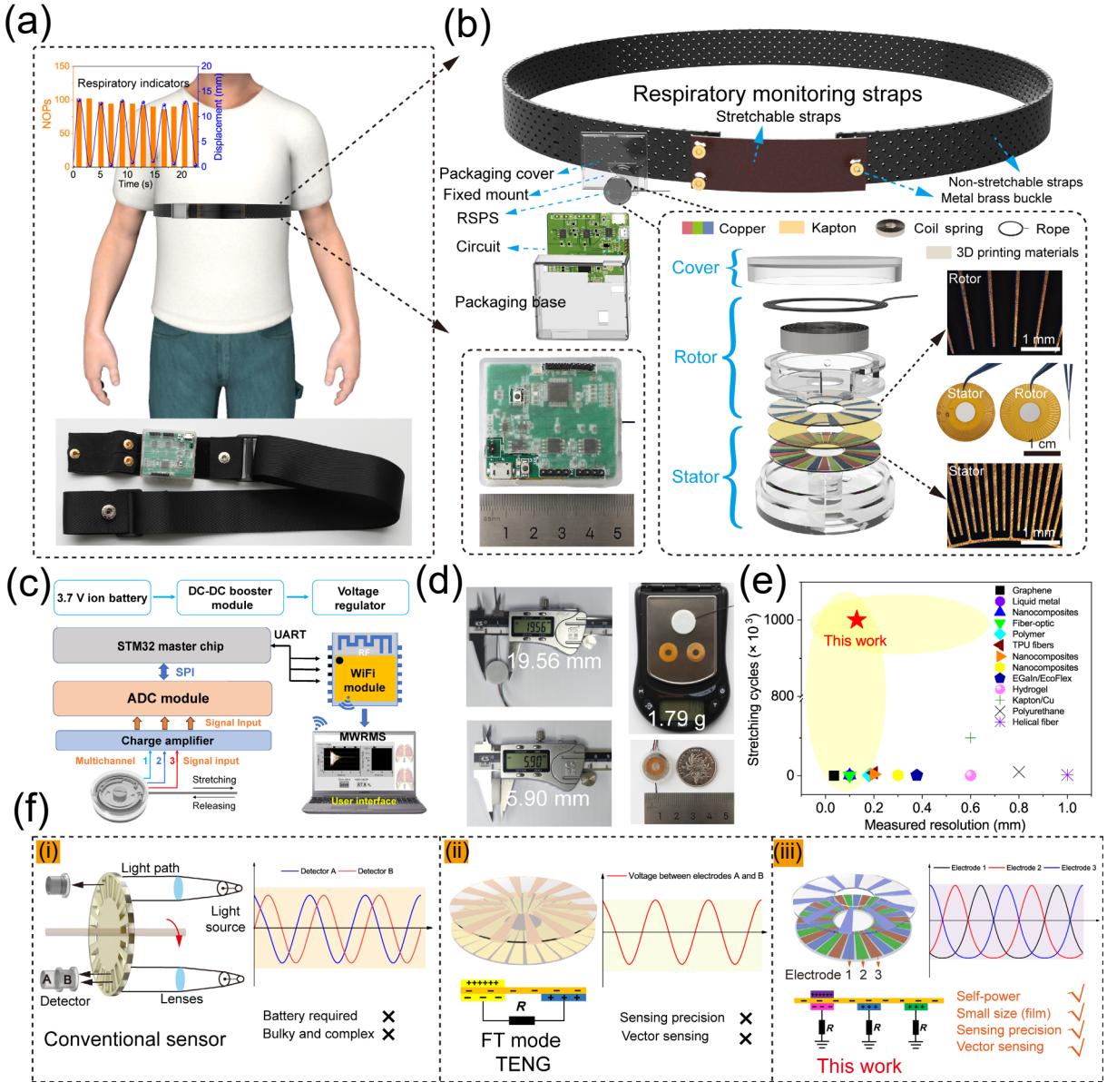

Figure 1 The concept, structure, and working principle of the whole system. (a) The diagram of the respiratory monitoring strap when worn, with the respiratory signals in the upper inset and the optical schematic of the chest strap in the lower inset. (b) Explosion diagrams of respiratory monitoring strap and RSPS. (c) Schematic diagram of the operational flow of the respiratory monitoring system. (d) The size and weight of RSPS. (e) Comparison of RSPS and stretchable sensors with different operating principles, including resistance, capacitance, triboelectricity, and optical and thermal effect sensors. (f) RSPS versus conventional sensors and FT mode TENG sensors.

experimentally. The RTF-TENG with a grid resolution of 1° and a radius of 7.6 mm was selected for output performance characterization via a program-controlled linear motor pull and signal acquisition by a matched multi-channel acquisition circuit, and displayed by a host computer (LabVIEW software). The sensor's output voltage at different stretching distances (from 1 to 10 mm) and speeds (from 0.01 to 0.1 m·s^{-1}) are shown in Figs. 2(d) and 2(e), respectively, exhibiting a maximum peak-to-peak voltage (V_{PP}) of 2.5 V. Furthermore, RTF-TENG with different electrode widths (1°, 2°, and 3°) was also characterized (more details of RTF-TENG are shown in Fig. S6 in the ESM), and the characterization results are shown in Fig. 2(f). The more detailed characterizations of RTF-TENG with different electrode widths are shown in Fig. S7 in the ESM, indicating that the narrower electrodes in the curves of the three electrode widths have faster response time and better precision under the same tensile distance. The RSPS also performed well for different stretch directions, as shown in Fig. 2(g). The sensor still has a stable voltage output when changing the stretch direction (0°–180° or −180°–0° in 30° steps) and controlling the same stretch distance. Compared to resistive, capacitive, piezoelectric, and other stretch devices with single-directional sensing [41, 42], RSPS demonstrates its multi-directional sensing capability.

In addition, it is known that the sensor's temperature and humidity largely determine the sensor's application range and prospect. Then, we tested the sensor in different temperature and humidity environments. The results in Figs. 2(h) (temperature ranging from 25 to 50 °C) and 2(i) (humidity ranging from 40% to 80%) show that increases in ambient temperature and humidity lead to a decrease in output voltage. Still, the corresponding NOPs and measurement distances remain stable (the temperature drift coefficient is nearly 700 ppm·°C^{-1}, Note S1 in the ESM), and this discrete sensing principle promotes the device's resistance to environmental interference.

2.3 RSPS as a digital and vector sensor

In this work, we utilized discrete sensing by counting the wave peaks and troughs, which are closely related to the sliding position

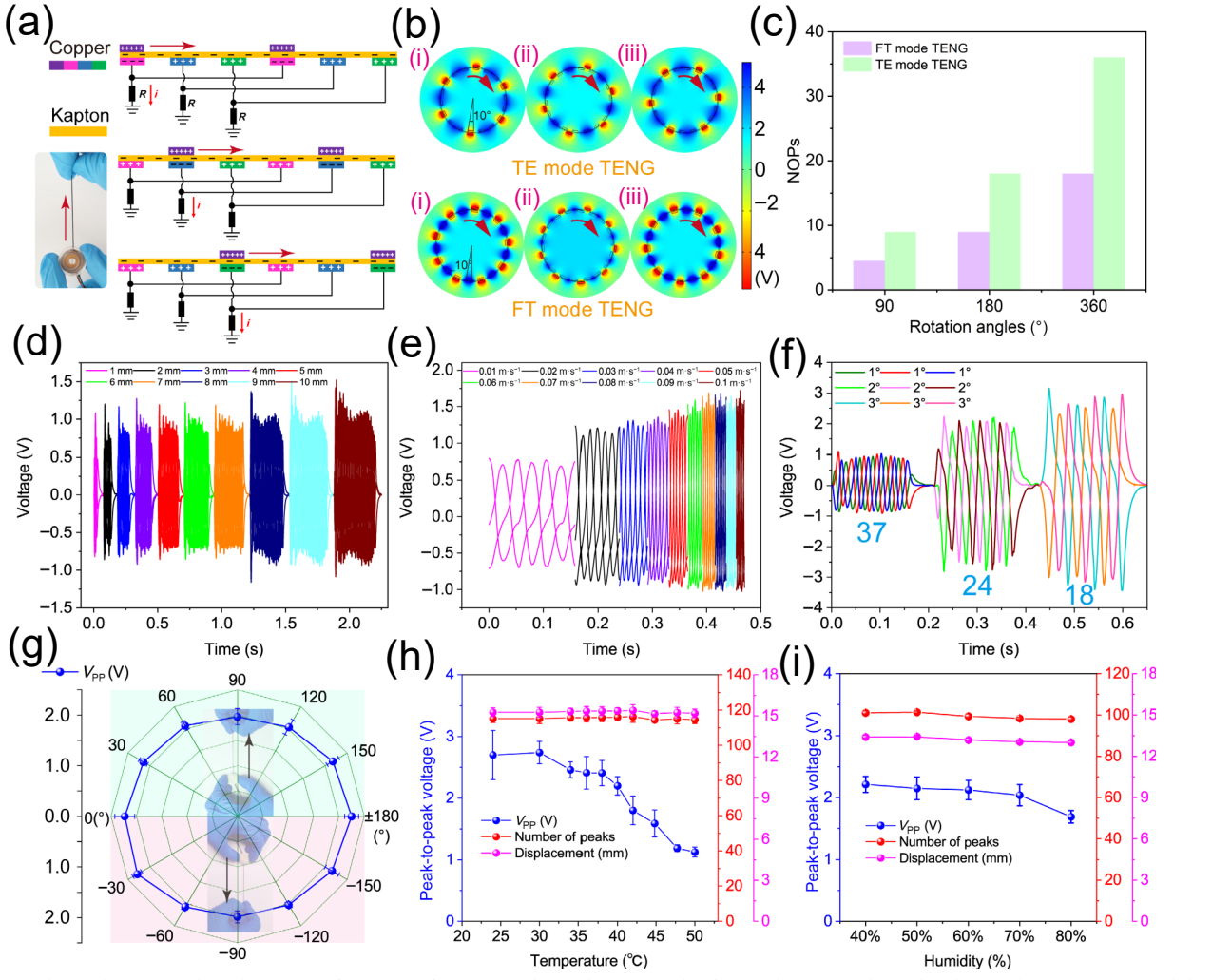

Figure 2 The working principle and output performances of RSPS. (a) The working principle of RSPS during stretching. (b) The simulation structures and the potential distributions of TE and FT modes TENG during rotation of 30°. (c) Resolution comparison of TE and FT modes TENG. (d) and (e) The output voltage of RSPS at different tensile displacements (from 1 to 10 mm) and speeds (from 0.01 to 0.1 m·s^{-1}). (f) Comparison of the output voltages of RTF-TENG with different electrode widths. (g) RSPS has sensing capability in a 180° stretch direction. (h) and (i) RSPS measurement results under different temperatures (from 25 to 50 ℃) and humidity environments (from 40% to 80%).

of the rotor relative to the stator. According to the analysis above, we explored the rotor position and waveform relative to the stator. In the simulation, for the TE and FT modes TENG, we set up a structure with equal width of rotor, stator, and stator gap to simulate the RSPS with 1° electrode width, and the results are shown in Fig. 3(a). When the rotor rotated 40°, the TENG in TE mode produced a total of four peaks (peaks plus troughs) with a simulation resolution of 10° and a sensitivity of 0.1 P·°$^{-1}$, while the TENG in FT mode generated a total of two peaks with a simulation accuracy of 20° and a sensitivity of 0.05 P·°$^{-1}$. Obviously, RTF-TENG based on TE mode can achieve higher resolution and sensitivity. More specifically, we performed tensile tests on RSPS with an electrode width of 1° utilizing a program-controlled linear motor, and the results are shown in Fig. 3(b). The controlled motor stretched 5 mm and produced about 37 peaks during stretching and contraction, and the following equation can calculate the tensile measurement displacement

$$L = \frac{\theta \pi R}{180} \tag{1}$$

where L represents displacement, R is the radius of RTF-TENG stator FPCB, and θ represents the total NOPs or rotation angle. The tensile measurement displacement calculated by the above equation (4.91 mm) is close to the set tensile displacement of 5 mm, demonstrating the high accuracy sensing capability of RSPS. Additionally, the RSPS has a vector sensing capability, with a phase difference between any two output waveform curves during stretching and contraction. As shown in the amplification curve at the bottom of Fig. 3(b), it is assumed to be positive when stretching and negative when releasing. The phase difference (α) between the two adjacent output waveforms during forward (α_1) and reverse (α_2) rotations can be expressed as

$$\alpha_1 = \frac{1}{3}\pi + 2n\pi, n = Z \tag{2}$$

and

$$\alpha_2 = \frac{2}{3}\pi + 2n\pi, n = Z \tag{3}$$

where Z represents integers. The displacement and phase differences of the device during stretching and releasing are shown in detail in Figs. S8 (displacement) and S9 (phase) in the ESM. The sensor also showed a low hysteresis as the linear motor was stretched and contracted, i.e., the NOPs when stretched are approximately equal to those when contracted (Movie ESM2). As shown in Fig. 3(c), the measured displacement and the displacement set by the linear motor essentially match via calculating NOPs, indicating that the device has excellent hysteresis, and the inset depicted a positive relationship between NOPs and the rotation angle (more details are available in Movie

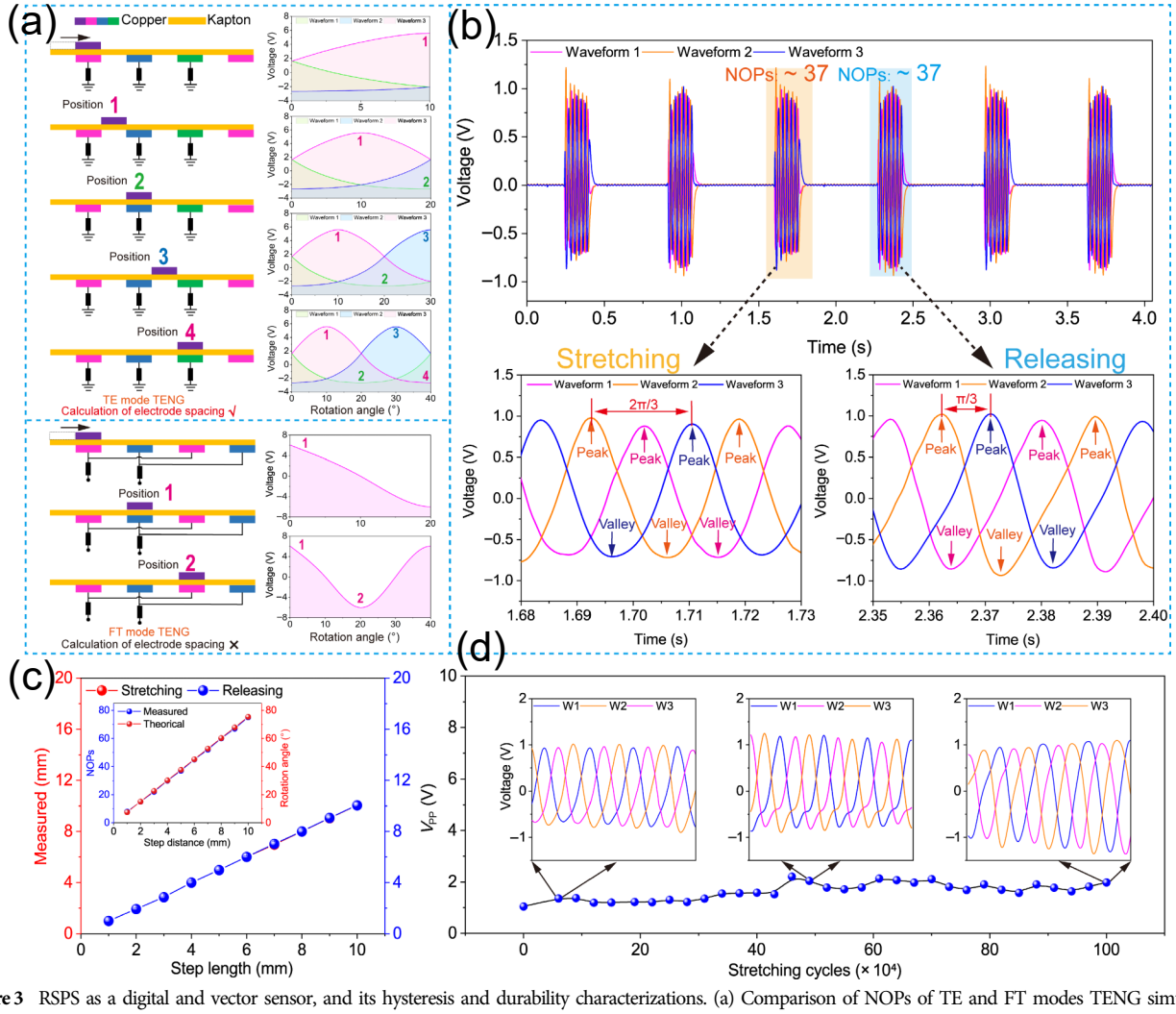

Figure 3 RSPS as a digital and vector sensor, and its hysteresis and durability characterizations. (a) Comparison of NOPs of TE and FT modes TENG simulated output when the rotor slides to different positions above the stator. (b) A linear motor drives the output curve of RSPS with a controlled stretching distance of 5 mm at a speed of 0.03 m·s^{-1}. The left and right enlarged graphs indicate the three sets of waveform curves with phase differences during stretching and contracting, respectively. (c) The hysteresis testing of RSPS. Inset represents the measured displacement, NOPs, and corresponding rotation angles of RSPS at different tensile displacements from 1 to 10 mm. (d) The robustness testing of RSPS.

ESM2). Similar results were found for the RSPS with different electrode widths (Fig. S10 in the ESM). Notably, we have also investigated the robustness of the sensor, as shown in Fig. 3(d), after 1 million continuous cycles of stretching, the high-temperature friction material kapton film and the package housing were largely intact (Fig. S11 in the ESM), and the RSPS still had a V_{PP} of 2 V, verifying its considerable stability.

2.4 Characterizations of respiratory parameters

When the human body breathes, the contraction and diastole of the diaphragm muscles cause the regular expansion and contraction of the thoracic cavity to exchange gas outward, and meet the needs of the body's metabolism (Fig. 4(a)). Respiratory movements often contain important physiological information, such as forced vital capacity (FVC), peak expiratory flow (PEF), forced expiratory volume in one second (FEV1), and RF [43, 44]. Hence, we developed the RSPS-based adjustable respiration monitoring belt, wrapped over the abdomen to monitor respiratory movements. The cure during the test subject's breathing is shown in Fig. 4(b), and the inset shows the optical photograph of the test and the waveform curve corresponding to one exhalation and one inhalation, where the NOPs and the amount of displacement change corresponding to this process are shown in Fig. 4(c). We also examined the influence of the belt on actual breathing activity. The results showed no obvious effect, as exhibited in Fig. 4(d). During exhalation, chest expansion leads to a gradual increase in the tensile displacement of the RSPS, with the maximum slope value of the tensile displacement reflecting the PEF (Fig. 4(e)), in agreement with the PEF curves measured by a commercial respiratory flowmeter (Fig. S12 in the ESM).

Furthermore, by using a commercial spirometer in parallel, we investigated the relationship between FEV1 and NOP in one second (NOP1), and that between FVC and NOPs, as shown in Figs. 4(f) and 4(g), respectively. Multiple results showed an obvious correlation between NOPs and expiratory volume, demonstrating the feasibility of RSPS for daily expiratory volume monitoring. Further, in medicine, the indicator of FEV1/FVC (one-second rate) is essential to measure the quality of lung function, indicating the presence of ventilatory dysfunction, or for diagnosing COPD, which is above 80% in normal people when there is no increase in airway resistance [45, 46]. Therefore, we compared the values of NOP1/NOPs and FEV1/FVC, as shown in Fig. 4(h), and found they matched well, suggesting the validity of our strap.

2.5 Multifunctional wearable respiratory monitoring system

In addition to quantifying the airflow per exhalation, the respiratory monitoring belt also needs to continuously real-time measure human respiration. As shown in Figs. 5(a)–5(c), the

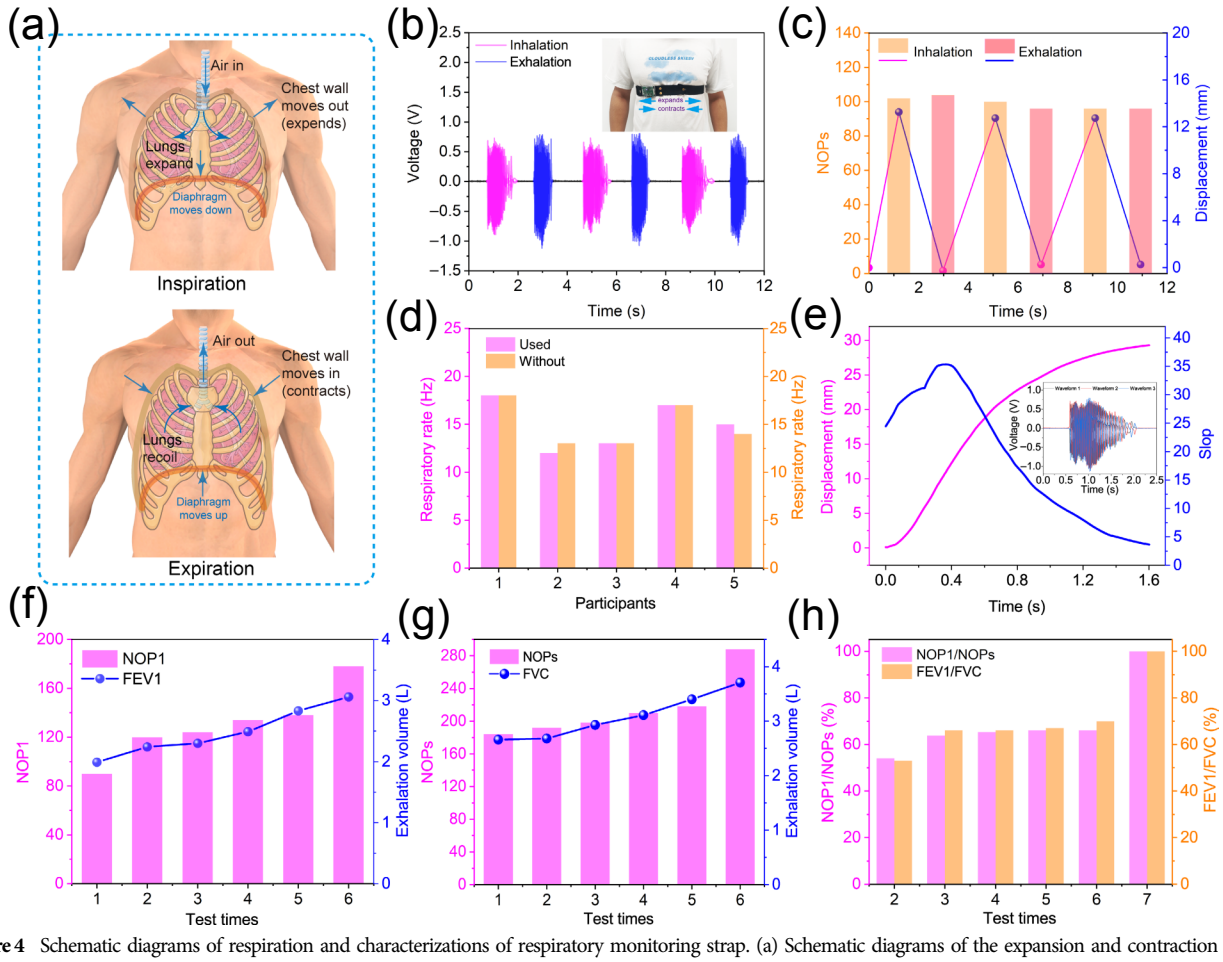

Figure 4 Schematic diagrams of respiration and characterizations of respiratory monitoring strap. (a) Schematic diagrams of the expansion and contraction of the thoracic diaphragm during human respiration. (b) Respiratory testing of the respiratory monitoring strap, where red represents inspiration and blue represents exhalation. (c) NOPs and corresponding displacement changes during exhalation and inhalation. (d) Respiratory monitoring strap enables monitoring of RF, with consistency in the RF obtained when worn and without it. (e) PEF test curves of RSPS, the inset represents the original waveform. (f) The FEV1 and NOP1, (g) FVC and NOPs, and (h) NOP1/NOPs and FEV1/FVC of RSPS under the two measurement methods.

output V_{PP} value, NOPs, and displacement changes were recorded for continuous breathing 200 s, rapid breathing (~ 30 Hz), and deep breathing (~ 15 Hz), respectively. Clearly, the stretch displacement and NOPs become larger but at a lower rate during deep breathing compared to normal or fast breathing.

More promisingly, owing to the considerable agreement between chest straps and commercial electronic spirometer results discussed previously, and the ability to sensing of multiple respiratory indicators, a MWRMS has been developed to continuously monitor of RF, one-second rate, apnea, and even apnea count. The schematic representation of the workflow and principle of MWRMS is shown in Fig. 5(d). Since the TE operating mode of RTF-TENG gives the sensor more functionality, thus signal characteristics such as phase difference, peak (or displacement), and threshold can be obtained by processing the signal at the terminal (LabVIEW upper computer) via custom algorithms. Then, by displaying the results of the above indications, we achieved real-time monitoring of RF, one-second rate, as well as apnea (detailed information can be found in Movie ESM3). MWRMS was applied to monitor RF, as shown in Fig. 5(e), where the inset represents a screenshot of the LabVIEW software interface. Additionally, since the NOP1/NOPs measured by our chest straps and FEV1/FVC measured by the commercial respiratory flowmeter match well, an approximation to the commercial respiratory flowmeter can be obtained by calculating the ratio of the number of respiratory waves in the previous second to the total NOPs, and the results are shown in Fig. 5(f).

It is worth noting that effective monitoring of apnea, a chronic disease widely prevalent worldwide, has become an essential part of respiratory monitoring sensors. By setting the threshold and apnea time, MWRMS can achieve the monitoring of apnea and apnea count. On one hand, when the wearer uses MWRMS and the respiratory pause time exceeds the set value, the respiratory monitoring terminal will generate an alarm alert (alarm light flashing). On the other hand, in addition to realizing the alarm for respiratory pause, MWRMS can also count respiratory pause to achieve continuous and meaningful respiratory pause monitoring, and Fig. 5(g) shows the data graphs of simulated respiratory pause. Meanwhile, for respiratory monitoring in different sleeping postures, MWRMS can also perform well, demonstrating the practicability of its daily monitoring (Fig. S13 in the ESM).

3 Conclusions

In summary, we have developed a RSPS with an easy-fabricate and lightweight structure, and high precision and excellent durability through a mature and mass-produced FPCB and 3D printing technology, and we forward-lookingly considered the industrial feasibility of the manufacturing technology of the whole system. Due to the RTF-TENG embedded inside the device, it not only endows it with the capability of vector sense but also doubles the sensing resolution compared to the traditional FT mode TENG. The comprehensively optimized RSPS has a stator area of only 1.2 cm^2, a sensing displacement resolution of 0.13 mm (sensing angle of 1°), a measurement sensitivity of 7 $P{\cdot}mm^{-1}$, and durability of 1 million continuous stretching cycles. Meanwhile,

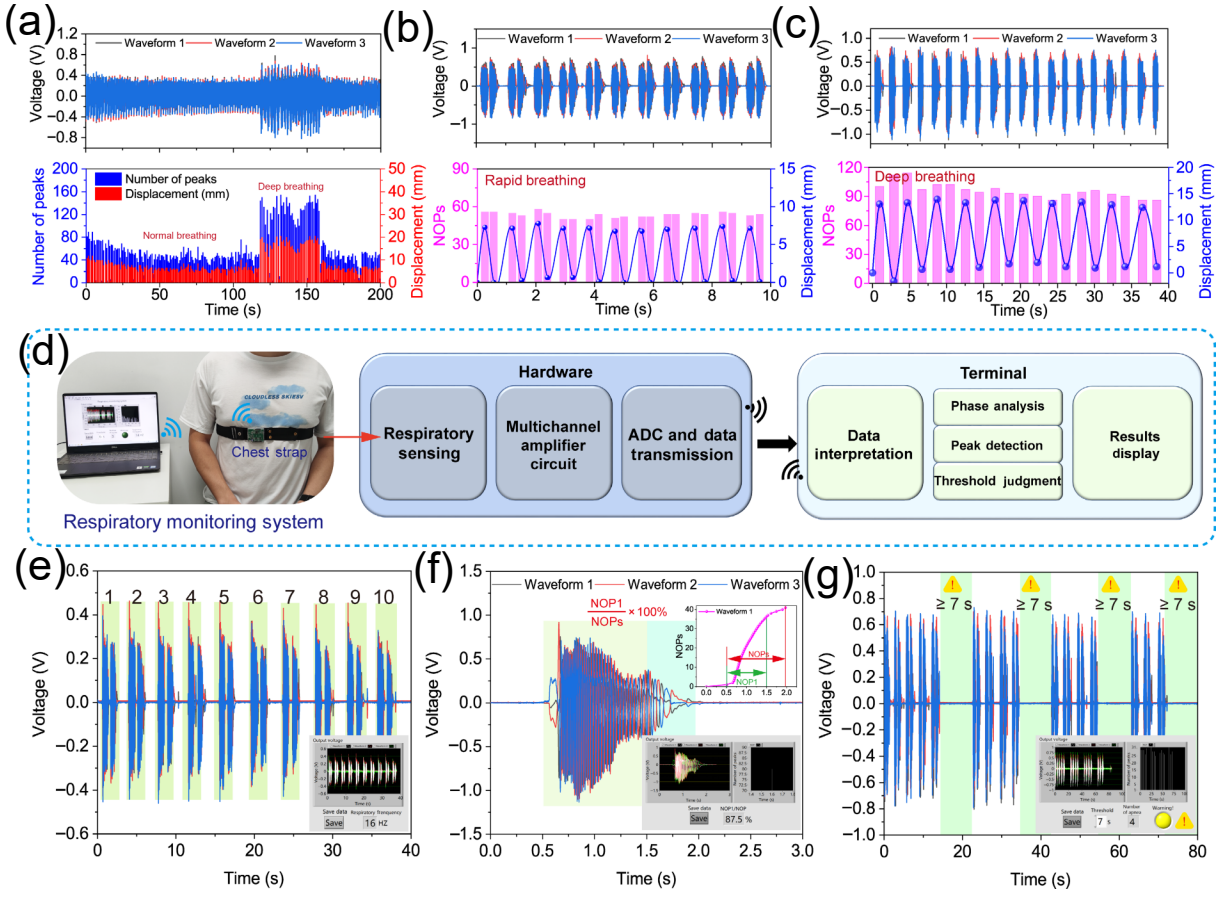

Figure 5 Set up of the MWRMS. The output waveforms, corresponding NOPs and displacement changes were recorded using respiratory monitoring strap for 200 s of (a) continuous breathing, (b) rapid breathing (~ 30 Hz), and (c) deep breathing (~ 15 Hz). (d) Schematic diagram of the overflow and principle of the MWRMS. The RSPS signals are acquired, processed, and sent through a multi-channel acquisition circuit, followed by real-time monitoring of multiple respiratory volumes at the terminal via analyzing the signals in phases, thresholds, and peak values. The MWRMS is applied for real-time wireless monitoring of (e) RF, (f) one-second rate, and (g) apnea.

the discrete measurement method gives the sensor ultralow hysteresis and immunity to environmental interference. On this basis, a comfortable, high-precision, and durable chest strap was developed for real-time monitoring of respiratory signals. Since the respiratory monitoring belt can sense multiple respiratory signals such as the wearer's expiratory volume, breathing intensity, RF, and apnea, a RSPS-based MWRMS has been proposed for effective monitoring of daily or home breathing. Experimental investigations have shown that the MWRMS can effectively monitor various important respiratory indicators such as RF, one-second rate, apnea, and apnea count, demonstrating its ability to be applied in personalized medicine and health monitoring.

4 Experimental section

4.1 Fabrications of RTF-TENG, RSPS, and respiratory monitoring belt

The design of the rotor and stator films of the RTF-TENG was drawn by Altium Designer 2018 software and processed by a mature double-layer FPCB fabrication and gold-sinking process, in which vias connected the electrodes of the upper and lower layers. RSPS was mainly composed of RTF-TENG, rotor, stator, and cover. Except for the fabrication of RTF-TENG introduced before, the rest of the rotor, stator, and cover were mainly processed by mature 3D printing technology (Object 30 Prime, Stratasys, USA). The preparation process of RSPS can be described as follows: Initially, the double-sided tape was cut with a laser cutter to have the same shape as the FPCB, and then it was taped to the rotor FPCB and the stator FPCB. Subsequently, the glued rotor and stator FPCBs were attached to the intermediate layers of the rotor and stator contacts, respectively, to form the complete friction structure. Finally, the whole RSPS package was prepared by embedding non-stretchable nylon rope and a coiled spring (size: Width and thickness are 1.8 and 0.13 mm, respectively). The preparation process of respiratory monitoring strap: With the connection and fixation of metal sub-buckles, stretchable and non-stretchable nylon straps were connected to each other, while one end of the rope in RSPS was fixed to one end of the stretchable nylon straps, and the other end was fixed to the RSPS device. Subsequently, an adjustable and wearable respiratory monitoring strap that can accurately measure the slight stretch was designed for respiratory monitoring.

4.2 Software and simulation

The data were calculated and processed using MATLAB 2020, LabVIEW 2018, and ORIGIN 2018. COMSOL Multiphysics 5.4 was used to perform finite element simulations of RTF-TENG. The simulation model used parametric scanning, point potential calculation, and network division in the electrostatic module. Moreover, the grid electrode widths in this simulation model were set to 10°, 20°, and 30°, the electrode gap was 10°, the diameter was about 20 mm, and the electrostatic field intermediary layer surface charge density was set to 2.319 e^{-8}·C·m^{-2}.

4.3 Characterization and measurement

The voltage measurement of the RSPS was mainly performed using a matched wireless multi-channel acquisition circuit,

including a power management module, a 16-bit AD acquisition module, a pre-charge amplifier, an ESP32 WiFi module, and a STM32L431 main control chip. The front-end amplifier amplified the signal and sent it to the AD chip for digitization, while the signal was sent to the data terminal via the WiFi module under the control of the master control chip (using 3 simultaneous sampling channels, each with a data sampling rate of 2 K·s^{-1}). Data terminals were received, displayed, and stored using a LabVIEW computer program (details of circuit diagram are depicted in Fig. S14 in the ESM). A linear motor (Linmot E1100) was used for tensile and durability testing of RSPS. And a cold field emission electron microscope (Hitachi SU8020) was used to observe the surface microstructure of Kapton films. Optical imaging of the RTF-FPCB was performed with a high-resolution optical microscope Marzhauser EK 75 × 50 Mot. Tango CZ EMV.

4.4 Respiratory monitoring system

Respiratory flow monitoring was collected simultaneously by a commercial spirometer and chest strap. The RSPS-based respiratory monitoring strap was applied to convert the expansion and contraction movements of the human chest during breathing into electrical signals, and the MWRMS was developed by a terminal (computer) using LabVIEW software. The results of RF, NOP1/NOPs (~ FEV1/FVC), apnea, and apnea count were visualized by analyzing and calculating the signals in real-time with algorithms such as phase analysis, peak detection, and threshold judgment on LabVIEW software. Volunteers approved the data collected in human participants study (respiratory signal detection) and the consent forms were signed.

Acknowledgements

This research was supported by the National Key Research and Development Program of China (No. 2021YFA1201601) and the National Natural Science Foundation of China (No. 52192610). We would like to thank Yanshuo Sun, Chuan Ning, and Jie An. for their helpful discussions. The volunteers involved in the respiratory monitoring are also the co-authors of this manuscript. No ethical approval was required in this case.

Electronic Supplementary Material: Supplementary material (additional figures and movies, including the production process of respiratory monitoring straps, the mechanical analysis of RSPS, RTF-TENG versus vector TENG sensors, the simulation studies of TE-TENG and FT-TENG, the additional characterization of RTF-TENG, the tensile and robustness tests of RSPS, the characterizations of the MWRMS during different sleeping positions, detailed circuit schematic of the MWRMS, the displacements and phase relations of RSPS, MWRMS for multifunctional respiratory monitoring) is available in the online version of this article at https://doi.org/10.1007/s12274-023-5420-1.

References

[1] Ferkol, T.; Schraufnagel, D. The global burden of respiratory disease. *Ann. Am. Thorac. Soc.* **2014**, *11*, 404–406.

[2] Nurmagambetov, T.; Kuwahara, R.; Garbe, P. The economic burden of asthma in the United States, 2008–2013. *Ann. Am. Thorac. Soc.* **2018**, *15*, 348–356.

[3] Guarascio, A. J.; Ray, S. M.; Finch, C. K.; Self, T. H. The clinical and economic burden of chronic obstructive pulmonary disease in the USA. *Clinicoecon. Outcomes Res.* **2013**, *5*, 235–245.

[4] Pekar, J.; Worobey, M.; Moshiri, N.; Scheffler, K.; Wertheim, J. O. Timing the SARS-CoV-2 index case in Hubei province. *Science* **2021**, *372*, 412–417.

[5] Cao, B.; Wang, Y. M.; Wen, D. N.; Liu, W.; Wang, J. L.; Fan, G. H.; Ruan, L. G.; Song, B.; Cai, Y. P.; Wei, M. et al. A trial of lopinavir-ritonavir in adults hospitalized with severe Covid-19. *N. Engl. J. Med.* **2020**, *382*, 1787–1799.

[6] Sachs, J. D.; Karim, S. S. A.; Aknin, L.; Allen, J.; Brosbøl, K.; Colombo, F.; Barron, G. C.; Espinosa, M. F.; Gaspar, V.; Gaviria, A. et al. The *Lancet* commission on lessons for the future from the COVID-19 pandemic. *Lancet* **2022**, *400*, 1224–1280.

[7] Liu, X. H.; Zhang, D. Z.; Wang, D. Y.; Li, T. T.; Song, X. S.; Kang, Z. J. A humidity sensing and respiratory monitoring system constructed from quartz crystal microbalance sensors based on a chitosan/polypyrrole composite film. *J. Mater. Chem. A* **2021**, *9*, 14524–14533.

[8] Chu, M.; Nguyen, T.; Pandey, V.; Zhou, Y. X.; Pham, H. N.; Bar-Yoseph, R.; Radom-Aizik, S.; Jain, R.; Cooper, D. M.; Khine, M. Respiration rate and volume measurements using wearable strain sensors. *NPJ Digit. Med.* **2019**, *2*, 8.

[9] Su, Y. J.; Chen, G. R.; Chen, C. X.; Gong, Q. C.; Xie, G. Z.; Yao, M. L.; Tai, H. L.; Jiang, Y. D.; Chen, J. Self-powered respiration monitoring enabled by a triboelectric nanogenerator. *Adv. Mater.* **2021**, *33*, 2101262.

[10] Fang, Y. S.; Xu, J.; Xiao, X.; Zou, Y. L.; Zhao, X.; Zhou, Y. H.; Chen, J. A deep-learning-assisted on-mask sensor network for adaptive respiratory monitoring. *Adv. Mater.* **2022**, *34*, 2200252.

[11] Zou, Y.; Gai, Y. S.; Tan, P. C.; Jiang, D. J.; Qu, X. C.; Xue, J. T.; Ouyang, H.; Shi, B. J.; Li, L. L.; Luo, D. et al. Stretchable graded multichannel self-powered respiratory sensor inspired by shark gill. *Fundam. Res.* **2022**, *2*, 619–628.

[12] Song, Y.; Min, J. H.; Yu, Y.; Wang, H. B.; Yang, Y. R.; Zhang, H. X.; Gao, W. Wireless battery-free wearable sweat sensor powered by human motion. *Sci. Adv.* **2020**, *6*, eaay9842.

[13] Chen, S. C.; Qian, G. C.; Ghanem, B.; Wang, Y. Q.; Shu, Z.; Zhao, X. F.; Yang, L.; Liao, X. Q.; Zheng, Y. J. Quantitative and real-time evaluation of human respiration signals with a shape-conformal wireless sensing system. *Adv. Sci.* **2022**, *9*, 2203460.

[14] Li, S.; Zhang, Y.; Liang, X. P.; Wang, H. M.; Lu, H. J.; Zhu, M. J.; Wang, H. M.; Zhang, M. C.; Qiu, X. P.; Song, Y. F. et al. Humidity-sensitive chemoelectric flexible sensors based on metal–air redox reaction for health management. *Nat. Commun.* **2022**, *13*, 5416.

[15] Chung, H. U.; Rwei, A. Y.; Hourlier-Fargette, A.; Xu, S.; Lee, K.; Dunne, E. C.; Xie, Z. Q.; Liu, C.; Carlini, A.; Kim, D. H. et al. Skin-interfaced biosensors for advanced wireless physiological monitoring in neonatal and pediatric intensive-care units. *Nat. Med.* **2020**, *26*, 418–429.

[16] Kumaravelu, D. P.; Govindasamy, K. Effect of prescribing and monitoring direct and indirect physical activity on selected health related fitness and cardio respiratory variables among obese school boys. *Int. J. Physiol. Nutr. Phys. Educ.* **2018**, *3*, 707–716.

[17] Roca, O.; Hernández, G.; Díaz-Lobato, S.; Carratalá, J. M.; Gutiérrez, R. M.; Masclans, J. R.; Spanish Multidisciplinary Group of High Flow Supportive Therapy in Adults. Current evidence for the effectiveness of heated and humidified high flow nasal cannula supportive therapy in adult patients with respiratory failure. *Crit. Care* **2016**, *20*, 109.

[18] Zhang, D. Z.; Xu, Z. Y.; Yang, Z. M.; Song, X. S. High-performance flexible self-powered tin disulfide nanoflowers/reduced graphene oxide nanohybrid-based humidity sensor driven by triboelectric nanogenerator. *Nano Energy* **2020**, *67*, 104251.

[19] Peng, X.; Dong, K.; Ning, C.; Cheng, R. W.; Yi, J.; Zhang, Y. H.; Sheng, F. F.; Wu, Z. Y.; Wang, Z. L. All-nanofiber self-powered skin-interfaced real-time respiratory monitoring system for obstructive sleep apnea–hypopnea syndrome diagnosing. *Adv. Funct. Mater.* **2021**, *31*, 2103559.

[20] Wang, D. Y.; Zhang, D. Z.; Li, P.; Yang, Z. M.; Mi, Q.; Yu, L. D. Electrospinning of flexible poly(vinyl alcohol)/MXene nanofiber-based humidity sensor self-powered by monolayer molybdenum diselenide piezoelectric nanogenerator. *Nano-Micro Lett.* **2021**, *13*, 57.

[21] Dassanayaka, D. G.; Alves, T. M.; Wanasekara, N. D.; Dharmasena, I. G.; Ventura, J. Recent progresses in wearable triboelectric nanogenerators. *Adv. Funct. Mater.* **2022**, *32*, 2205438.

[22] Li, Z.; Zheng, Q.; Wang, Z. L.; Li, Z. Nanogenerator-based self-powered sensors for wearable and implantable electronics. *Research* **2020**, *2020*, 8710686.

[23] Zhao, Z. Z.; Yan, C.; Liu, Z. X.; Fu, X. L.; Peng, L. M.; Hu, Y. F.; Zheng, Z. J. Machine-washable textile triboelectric nanogenerators for effective human respiratory monitoring through loom weaving of metallic yarns. *Adv. Mater.* **2016**, *28*, 10267–10274.

[24] Wang, D. Y.; Zhang, D. Z.; Yang, Y.; Mi, Q.; Zhang, J. H.; Yu, L. D. Multifunctional latex/polytetrafluoroethylene-based triboelectric nanogenerator for self-powered organ-like MXene/metal-organic framework-derived CuO nanohybrid ammonia sensor. *ACS Nano* **2021**, *15*, 2911–2919.

[25] Wang, D. Y.; Zhang, D. Z.; Chen, X. Y.; Zhang, H.; Tang, M. C.; Wang, J. H. Multifunctional respiration-driven triboelectric nanogenerator for self-powered detection of formaldehyde in exhaled gas and respiratory behavior. *Nano Energy* **2022**, *102*, 107711.

[26] Zhang, D.; Xu, S. W.; Zhao, X.; Qian, W. Q.; Bowen, C. R.; Yang, Y. Wireless monitoring of small strains in intelligent robots via a joule heating effect in stretchable graphene-polymer nanocomposites. *Adv. Funct. Mater.* **2020**, *30*, 1910809.

[27] Liu, X. B.; Liang, X. W.; Lin, Z. Q.; Lei, Z. M.; Xiong, Y. X.; Hu, Y. G.; Zhu, P. L.; Sun, R.; Wong, C. P. Highly sensitive and stretchable strain sensor based on a synergistic hybrid conductive network. *ACS Appl. Mater. Interfaces* **2020**, *12*, 42420–42429.

[28] Peng, X.; Dong, K.; Ye, C. Y.; Jiang, Y.; Zhai, S. Y.; Cheng, R. W.; Liu, D.; Gao, X. P.; Wang, J.; Wang, Z. L. A breathable, biodegradable, antibacterial, and self-powered electronic skin based on all-nanofiber triboelectric nanogenerators. *Sci. Adv.* **2020**, *6*, eaba9624.

[29] Wang, D. Y.; Zhang, D. Z.; Guo, J. Y.; Hu, Y. Q.; Yang, Y.; Sun, T. H.; Zhang, H.; Liu, X. H. Multifunctional poly(vinyl alcohol)/Ag nanofibers-based triboelectric nanogenerator for self-powered MXene/tungsten oxide nanohybrid NO_2 gas sensor. *Nano Energy* **2021**, *89*, 106410.

[30] Nankali, M.; Nouri, N. M.; Navidbakhsh, M.; Malek, N. G.; Amindehghan, M. A.; Shahtoori, A. M.; Karimi, M.; Amjadi, M. Highly stretchable and sensitive strain sensors based on carbon nanotube-elastomer nanocomposites: The effect of environmental factors on strain sensing performance. *J. Mater. Chem. C* **2020**, *8*, 6185–6195.

[31] Zhu, H. Y.; Wang, S. L.; Zhang, M. H.; Li, T. Y.; Hu, G. H.; Kong, D. S. Fully solution processed liquid metal features as highly conductive and ultrastretchable conductors. *npj Flex. Electron.* **2021**, *5*, 25.

[32] Yu, Y. F.; Zheng, G. C.; Dai, K.; Zhai, W.; Zhou, K. K.; Jia, Y. Y.; Zheng, G. Q.; Zhang, Z. C.; Liu, C. T.; Shen, C. Y. Hollow-porous fibers for intrinsically thermally insulating textiles and wearable electronics with ultrahigh working sensitivity. *Mater. Horiz.* **2021**, *8*, 1037–1046.

[33] Zhang, Y. Y.; Huang, Y.; Liu, P.; Liu, C. X.; Guo, X. H.; Zhang, Y. G. Highly stretchable strain sensor with wide linear region via hydrogen bond-assisted dual-mode cooperative conductive network for gait detection. *Compos. Sci. Technol.* **2020**, *191*, 108070.

[34] Xia, M.; Pan, S. X.; Li, H. H.; Yi, X.; Zhan, Y.; Sun, Z. G.; Jiang, X. L.; Zhang, Y. H. Hybrid double-network hydrogel for highly stretchable, excellent sensitive, stabilized, and transparent strain sensors. *J. Biomater. Sci. Polym. Ed.* **2021**, *32*, 1548–1563.

[35] Kim, S.; Yoo, B.; Miller, M.; Bowen, D.; Pines, D. J.; Daniels, K. M. EGaIn-silicone-based highly stretchable and flexible strain sensor for real-time two joint robotic motion monitoring. *Sens. Actuators A Phys.* **2022**, *342*, 113659.

[36] Ning, C.; Cheng, R. W.; Jiang, Y.; Sheng, F. F.; Yi, J.; Shen, S.; Zhang, Y. H.; Peng, X.; Dong, K.; Wang, Z. L. Helical fiber strain sensors based on triboelectric nanogenerators for self-powered human respiratory monitoring. *ACS Nano* **2022**, *16*, 2811–2821.

[37] Liu, H.; Zhang, S. M.; Li, Z. K.; Lu, T. J.; Lin, H. S.; Zhu, Y. Z.; Ahadian, S.; Emaminejad, S.; Dokmeci, M. R.; Xu, F. et al. Harnessing the wide-range strain sensitivity of bilayered PEDOT:PSS films for wearable health monitoring. *Matter* **2021**, *4*, 2886–2901.

[38] Li, C. C.; Zhou, B. Z.; Zhou, Y. F.; Ma, J. W.; Zhou, F. L.; Chen, S. J.; Jerrams, S.; Jiang, L. Carbon nanotube coated fibrous tubes for highly stretchable strain sensors having high linearity. *Nanomaterials* **2022**, *12*, 2458.

[39] Li, C. Y.; Liu, D.; Xu, C. Q.; Wang, Z. M.; Shu, S.; Sun, Z. R.; Tang, W.; Wang, Z. L. Sensing of joint and spinal bending or stretching via a retractable and wearable badge reel. *Nat. Commun.* **2021**, *12*, 2950.

[40] Bai, H. D.; Li, S.; Barreiros, J.; Tu, Y. Q.; Pollock, C. R.; Shepherd, R. F. Stretchable distributed fiber-optic sensors. *Science* **2020**, *370*, 848–852.

[41] Chen, X. L.; Li, X. M.; Shao, J. Y.; An, N. L.; Tian, H. M.; Wang, C.; Han, T. Y.; Wang, L.; Lu, B. H. High-performance piezoelectric nanogenerators with imprinted P(VDF-TrFE)/$BaTiO_3$ nanocomposite micropillars for self-powered flexible sensors. *Small* **2017**, *13*, 1604245.

[42] Leber, A.; Dong, C. Q.; Chandran, R.; Das Gupta, T.; Bartolomei, N.; Sorin, F. Soft and stretchable liquid metal transmission lines as distributed probes of multimodal deformations. *Nat. Electron.* **2020**, *3*, 316–326.

[43] Torén, K.; Schiöler, L.; Lindberg, A.; Andersson, A.; Behndig, A. F.; Bergström, G.; Blomberg, A.; Caidahl, K.; Engvall, J. E.; Eriksson, M. J. et al. The ratio FEV1/FVC and its association to respiratory symptoms—A Swedish general population study. *Clin. Physiol. Funct. Imaging* **2021**, *41*, 181–191.

[44] Chiry, S.; Cartier, A.; Malo, J. L.; Tarlo, S. M.; Lemière, C. Comparison of peak expiratory flow variability between workers with work-exacerbated asthma and occupational asthma. *Chest* **2007**, *132*, 483–488.

[45] Lambert, A.; Drummond, M. B.; Wei, C.; Irvin, C.; Kaminsky, D.; McCormack, M.; Wise, R. Diagnostic accuracy of FEV1/forced vital capacity ratio z scores in asthmatic patients. *J. Allergy Clin. Immunol.* **2015**, *136*, 649–653.e4.

[46] GBD 2015 Chronic Respiratory Disease Collaborators. Global, regional, and national deaths, prevalence, disability-adjusted life years, and years lived with disability for chronic obstructive pulmonary disease and asthma, 1990–2015: A systematic analysis for the global burden of disease study 2015. *Lancet Resp. Med.* **2017**, *5*, 691–706.